이학석사 학위논문

2D 반데르발스 반강자성 MPS_3 (M=Mn, Co, and Fe)를 기반으로 한 스핀 칼로리트로닉 소자에 관한 연구

Investigation of Spin Caloritronic Devices Based on 2D van der Waals Antiferromagnetic MPS_3 (M=Mn, Co, and Fe)

울산대학교 대학원

화 학 과

시 우 진

Investigation of Spin Caloritronic Devices Based on 2D van der Waals Antiferromagnetic MPS_3 (M=Mn, Co, and Fe)

지도교수 이 승 구

이 논문을 이학석사학위 논문으로 제출함

2024년 2월

울 산 대 학 교 대 학 원

화 학 과

시 우 진

Table of Contents

List of Figures

초 록

스핀칼로리트로닉스는 스핀트로닉스, 열전, 그리고 열자기를 혼합한 신흥 분야이며, 저차원 시스템에서 높은 전환 효율을 달성할 수 있는 새로운 가능성을 제공한다. 열전소자는 온도 구배로부터 전압을 발생시키는 제벡 효과를 이용하는 반면에, 스핀칼로리트로닉스 물질은 스핀과 순수 스핀 전류를 발생시키는 열적 유도된 스핀 제벡 효과를 이용한다. 스핀 제벡 효과를 통한 스핀 각 운동량 또는 자기 모멘트의 흐름인 스핀 전류는 향상된 에너지 효율을 갖는 전하 전류의 잠재적인 대체재로써 최근 주목받고있다. 금속 시스템에서는 스핀 분극 전도 전자가 스핀 전류의 운반체인 반면, 절연 시스템에서는 스핀파 스핀 전류가 스핀 전류의 운반체이다. 특히, 스핀파 스핀 전류가 훨씬 더 긴 붕괴 길이를 가지며, 전하 전류의 흐름과 줄 발열의 손실을 동시에 피할 수 있으므로, 스핀트로닉스에 대한 강한 장점을 가지고 있다. 그러나, 대부분 자기 절연체는 반강자성인 경향이 있고, 그래서 반강자성체에서 스핀파가 스핀 전류를 운반할지 아닌지에 대한 여부는 중요한 질문이다. 최근, S. Seki 외 연구진들은 반강자성 절연체가 고유한 스핀트로닉 기능을 가지는 유망한 소스임을 강조하며, 반강자성 스핀파가 스핀 전류의 효율적인 운반체가 될 수 있음을 보여주었다. 본 연구에서, 우리는 스핀 발생기로써 2D 반 데르 발스 반강자성 MPS_3 자기 절연체를, 스핀 검출기로써 Pt, Ta, 그리고 W과 같은 중금속 (θ_{SH} in Pt, Ta, and W are in range of ~0.012 to ~0.15 and ~0.33) 또는 Bi_2Se_3 등과 같은 위상 절연체 (θ_{SH} in Bi_2Se_3 varying from 0.01 to 3.5)를 사용하여 스핀 제벡 효과를 연구하는 것을 목표로 한다.

Abstract

Spin-caloritronics is an emerging field that combines spintronics, thermoelectrics (TEs), and thermomagnetics, offering new possibilities for achieving high conversion efficiencies in low-dimensional systems. While TE devices (thermopiles) use the Seebeck effect to generate a voltage from a temperature gradient, spin-caloritronics materials use the thermally induced spin Seebeck effect (SSE), which generates the spin and pure spin current. Spin current, i.e., a flow of spin angular momentum or

magnetic moment via SSE, has recently attracted renewed attention as a potential alternative to charge current with improved energy efficiency. In metallic systems, the spin-polarized conduction electrons are the carriers of the spin current, whereas in insulating systems the spin-wave spin current (SWSC) is the carrier of the spin current. In particular, the spin-wave spin current (SWSC) has a much longer decay length and avoids the simultaneous flow of charge current and Joule heat loss, a strong advantage for spintronics. However, most magnetic insulators tend to be antiferromagnetic, and it is a critical question whether the spin waves in antiferromagnets can carry a spin current or not. Recently, S. Seki et al. have shown that the antiferromagnetic spin wave can be an efficient carrier of spin current, highlighting antiferromagnetic insulators as a promising source of unique spintronic functions. In this research work, we aim to investigate SSE using 2D vdW antiferromagnetic (AFM) MPS_3 (M=Mn or Co) magnetic insulator as spin generator and heavy metal e.g. Pt, Ta, W, etc. (θ_{SH} in Pt, Ta, and W are in range of ~0.012 to ~0.15 and ~0.33) or topological insulator e.g. Bi2Se3, etc. (θ_{SH} in Bi_2Se_3 varying from 0.01 to 3.5) as a spin detector.

Keywords: Spintronics; Spin caloritronics; Spin Seebeck effect; Inverse spin Hall effect; 2D material; Antiferromagnetic; Spin-wave spin current; MPS_3; Transition metal phosphorus trisulfide

1. Introduction

Nowadays, interest in energy harvesting and energy recycling is rising because previously used energy has been exhausted. There are a lot of useful energy sources that originate from heat, light, and electromagnetic wave[1]. One of the above energy sources, thermoelectric generators (TEGs) using the Seebeck effect to generate a voltage from a temperature gradient are attracting methods because thermoelectric generators can use both artificial heat including waste heat from industry and natural heat. Unlike other heat sources, there are many sources available since heat is unavoidably produced in many industries. Even converting other heat sources to voltage always produces waste heat. The efficiency of the thermoelectric generation by the Seebeck effect can be represented by the dimensionless figure of merit $Z\bar{T}$, defined as

$$Z\bar{T} = \frac{\alpha^2}{\kappa\rho}\bar{T}$$

where κ, ρ, $\bar{T}$, and α are thermal conductivity, electrical resistivity, average temperature between the hot and cold ends, and Seebeck coefficient[2]. However, conventional thermoelectric devices could generate only a few levels of voltage[3]. So, it is important to increase the efficiency of thermoelectric generators. To increase the efficiency of thermoelectric generators, there are two ways to improve $Z\bar{T}$. One is increasing the Seebeck coefficient, and another is decreasing thermal conductivity and electrical resistivity together. But there is a physical limitation to improving $Z\bar{T}$. According to the Wiedmann-Franz law, the product of the electronic thermal conductivity and the electrical resistivity is constant and characterized by the Lorenz number L_e, below as

$$\kappa_e\rho = L_eT$$

This limitation is present in all isotropic metals where the electronic part κ_e of the thermal conductivity dominates. For this reason, it was a challenge to control completely independent of thermal conductivity and electrical resistivity.

After the first discovery of the giant magnetoresistance (GMR) effect, which is called the origin of spintronics, in the late 1980s[4], a spin-dependent counterpart of the Seebeck effect called the "Spin Seebeck effect" was also discovered[5]. Spin Seebeck effect (SSE) is the generation of a spin and pure spin current from a temperature gradient in a magnetic material[6, 7]. Spin current will be explained below in the mechanism of SSE devices. This discovery of the spin Seebeck effect caused a new research field of Spin-Caloritronics. Spin caloritronics converts from the heat current to the charge current mediated by the spin[8]. Similar to SSE, there is the same interaction between heat and electrical energy called the Anomalous Nernst effect (ANE)[9, 10]. ANE generates a thermoelectric voltage transverse to the imposed temperature gradient and applied magnetic field in ferromagnets or antiferromagnets without a conducting layer. ANE can give rise to a large Nernst thermopower at a low magnetic field. High magnetization and strong inherent stray field of ferromagnets introduce a strong magnetic disturbance. So, it is why ANE is not useful for ferromagnets.

Also, for the spin caloritronic device, by injecting the spin current into an adjacent conductive film, the spin current can be converted into a charge current through the inverse spin Hall effect[11-13]. This inverse spin Hall effect could be represented by the conversion from the spin current to the charge current via generated voltage. Since the conversion from heat to spin current can occur in magnetic materials and conversion of the charge current occurs in an adjacent conductor, it would allow decoupling of the thermal conductivity and electrical

resistivity. For this reason, the introduction of spin caloritronics could not only improve the efficiency in TEGs but also engineer the material properties of SSE devices. Nowadays, these types of spin caloritronic devices have been applicated for magneto-thermoelectric[12], which include heaters using the spin Seebeck effect or coolers using the spin Peltier effect and magnonic application[14].

For more detail, the mechanism of spin caloritronic devices also called SSE devices consisting of a magnetic layer and a conducting layer below as:

1. Conversion from a thermal gradient to a spin current which magnons (spin wave) can carry in the magnetic material via the Spin Seebeck effect (SSE). In this paper, we will consider this magnetic material to be an antiferromagnetic insulator. Consequently, the currents will be carried by magnons.
2. Interfacial exchange interaction at the interface between the magnetic layer (ML) and the conducting layer (CL) via spin-mixing conductance. In this part, we will only consider the conversion from a magnon spin current in the magnetic layer to a conduction electron spin current in the conducting layer. The basic principle behind the spin-mixing conductance relies on spin transfer torque (STT), where spin currents can move magnetizations. With the thermal-induced magnon spin currents, magnons are accumulated at the ML/CL interface. Magnons will diffuse into the CL where the magnetization relaxes characterized by its relaxation length.
3. Conversion from a spin current to a charge current where conduction electrons will carry in the CL via inverse spin Hall effect (ISHE). The originally discovered Spin Hall effect describes the conversion of a charge current $\boldsymbol{J}_c$ to a spin current $\boldsymbol{J}_S$ in materials with high spin-orbit interaction,

$$\boldsymbol{J}_c = \theta_{SH}\hat{\mathbf{s}} \times \boldsymbol{J}_S$$

with θ_{SH} is the spin Hall angle, and $\hat{\mathbf{s}}$ is the unit vector pointing along the electron-spin polarization in the conducting layer. The opposite conversion from a spin current to a charge current can also occur through the same mechanism, named the inverse spin Hall effect (ISHE)

$$\boldsymbol{J}_S = \theta_{SH}\hat{\mathbf{s}} \times \boldsymbol{J}_C$$

Therefore, if the CL is chosen accordingly to have a large spin-orbit interaction to induce the inverse spin Hall effect, it is possible to convert the spin current to a charge current. The generated electric field in the CL due to the charge current is then given by

$$E_{ISHE} = (\theta_{SH}\rho)\hat{\mathbf{s}} \times \boldsymbol{J}_C$$

where ρ is the electrical resistivity of the CL. The generated electrical field is therefore also dependent on the magnetization direction of the spin current. So, ISHE enables spin currents to be detected indirectly as voltage signals.

By combining all three mechanisms: spin current generation carried by magnons due to a thermal gradient in the ML, spin-mixing conductance at the ML/CL interface, and spin current to charge current conversion by the ISHE in the CL; it is possible to generate an electrical field – the spin Seebeck effect.

The first experimental discovery of the SSE was shown by Uchida et al. in 2008

with a combination of $Ni_{81}Fe_{19}$ ferromagnet and Pt[5]. They showed a Seebeck coefficient $\alpha = 2\ nVK^{-1}$ at 300 K. It was also developed with a combination of $Y_3Fe_5O_{12}$ (YIG) ferrimagnet with Pt and this combination is an excellent setup for pure spin detection of spin current effect and thereby one of the most studied SSE systems[2, 15, 16]. This Pt/YIG showed a Seebeck coefficient $\alpha = 4.5\ \mu VK^{-1}$. Like the above devices, most of the reported devices consist of either ferrimagnets or ferromagnets ML, with a Seebeck coefficient range of only a value of a few Kelvin. However, antiferromagnets are less studied than others but can improve the SSE efficiency in the devices. Devices consisting of antiferromagnetic MnF_2 insulators have been shown to produce SSE signals, with improved performance at low temperatures (5~50 K), and having Seebeck coefficients as high as $41.2\ \mu VK^{-1}$ in the presence of an external magnetic field[6, 17]. In this regard, we chose antiferromagnets as a magnetic layer to enhance the SSE efficiency in spin caloritronic devices.

MPX_3, one of the transition metal phosphorus trichalcogenides (TMPTs) is an emerging 2D van der Waals antiferromagnetic material[18-20]. For the chemical structure, M = transition metal (M=Mn, Co, Fe, Ni, Cd, etc.), P = phosphorus and X = chalcogenides (X=S, Se or Te). Flakes with MPX_3 structure can be easily mechanically exfoliated because its layers have weak van der Waals (vdW) force in the out-of-plane direction, unlike strong covalent bonds for in-plane direction[21]. MPX_3 has some advantages e.g., 2D vdW, antiferromagnetism, and insulator[22]. Layered MPX_3 exhibits a number of improved properties compared to their bulk counterparts due to their band gap, 1.3 to 3.5 eV[23]. These improved properties originate from its layered structure. Also, the reason why MPX_3 should be investigated is the insulating property as well as a tunable band gap. Insulating MPS_3 can reduce the leakage of current in devices, so by adopting MPS_3 as a magnetic material in spin caloritronic devices, we can anticipate an improvement in efficiency. These antiferromagnetic materials have a critical temperature, called Néel temperature (T_N)[24]. Antiferromagnets exist as antiferromagnetic materials only below T_N. If the temperature goes high, these

materials are paramagnets due to thermal fluctuation. So, it is important to keep the temperature below T_N or observe the temperature change go through T_N for the devices. However, most magnetic insulators tend to be antiferromagnetic[6], and it is a critical question whether the spin waves in antiferromagnets can carry a spin current or not. Recently, S. Seki et al. have shown that the antiferromagnetic spin wave can be an efficient carrier of spin current, highlighting antiferromagnetic insulators as a promising source of unique spintronic functions.

In general, heavy metals (HMs) have been used as spin detectors in spin caloritronic devices because HMs have strong spin-orbit coupling[25]. Generated spin currents and E_{ISHE} are correlate to the spin Hall angle (θ_{SH}), so using HMs having more higher θ_{SH} would be helpful to get more efficient devices. Among them, W has a larger spin Hall angle (θ_{SH}) value of ~0.50[26] compared to other heavy metal Pt (~0.012) and Ta (~0.15)[27]. That is why we selected W as a conducting material in spin caloritronic devices.

Furthermore, there is another candidate for the conducting layer, it is topological insulators (TIs)[28-30]. TI is a material whose interior behaves as an electrical insulator while its surface behaves as an electrical conductor. The first reported 2D TI using the quantum Hall effect needed a magnetic field[31]. So, internal electrons moving is confined in a circular direction and the external electrons move in one direction. Then, 2D TI using the quantum spin Hall effect needed a material having high spin-orbit coupling without any additional magnetic field[32]. In these 2D TI systems, the energy level exists on the surface, and the energy level is located between the bulk band gaps. A new concept of 3D TI was reported, it consists of a body state with an insulating band gap, and a surface state without a band gap[33]. In this 3D TI system, the surface state can exist stably due to the protection of the time-reversal symmetry. Bi_2Se_3, for example, is one of the promising TI having a band gap of 0.2

to 0.3 eV[34]. Bi_2Se_3 consists of a quintuple layer (Se-Bi-Se-Bi-Se) and the van der Waals gap exists between each quintuple layer[35]. Bi_2Se_3 film can be fabricated by magnetron sputtering, chemical vapor deposition, and electrodeposition methods. Among them, the molecular beam epitaxy (MBE) method can make the single crystal film at standard stoichiometric ratios[36]. The spin direction of the surface state is always perpendicular to the direction of momentum due to the spin-coupling effect. So, electrons travel on the surface with low loss or lossless at a speed like photons. In this regard, this kind of TI has excellent surface mobility ($\mu s \sim 6000\ cm^2/Vs$)[37].

In this paper, we report spin caloritronic devices of W/MPS_3 structure to investigate SSE and ISHE. We aimed antiferromagnetic behavior of MPS_3 via temperature change, and conversion of thermally induced spin-wave spin current (SWSC) to charge current. MPS_3 has been easily attached to the Si/SiO_2 using mechanical exfoliation and digital masks have been fabricated for E-beam lithography (EBL), then deposited W on the MPS_3. Antiferromagnetic MPS_3 has been analyzed using Raman spectroscopy to investigate magnetic phase transition near T_N where temperature changes. This is the first report for a combination of antiferromagnetic MPS_3 and W to explore the ISHE. We believe our research could help enhance the efficiency of spin caloritronic devices as well as overcome energy problems.

2. Experimental Section

2. 1. Materials

2. 1. 1. Spin Generators: $MnPS_3$, $CoPS_3$, and $FePS_3$

The magnetic layer for the SSE devices in this thesis consists of 2D antiferromagnetic transition-metal phosphorus trisulfide structures of the MPS_3 (M = Mn, Co, and Fe). Each was purchased from *2Dsemiconductors USA*.

$MnPS_3$ is the 2D van der Waals material and it has the exfoliability. It has a monoclinic C2/m crystal space group, with lattice parameters a = 6.077 Å, b = 10.524 Å, c = 6.796 Å, and β = 107.35°. Also, it has an out-of-plane antiferromagnetic ordering which can be described by the Heisenberg model on a honeycomb lattice, with a Néel temperature of T_N = 78 K and a spin-flop transition at $\mu_0 H \cong 5\ T$.

2D XY-type $CoPS_3$ is very similar to $MnPS_3$ with the same monoclinic C2/m space group, and lattice parameters a = 5.901 Å, b = 10.222 Å, c = 6.658 Å, and β = 107.58°. Similarly, $CoPS_3$ can be used exfoliated due to the weak van der Waals force for out-of-plane direction. Contrary to $MnPS_3$, $CoPS_3$ has an in-plane magnetization direction with a slightly higher Néel temperature of T_N = 120 K.

$FePS_3$ is another one with a 2D Ising model on a honeycomb lattice having a monoclinic structure with the space group C/m. Its lattice parameters are a = 5.947 Å, b = 10.300 Å, c = 6.722 Å, and β = 107.16° and T_N = 123 K. Spins are aligned along with the out-of-plane direction Like $MnPS_3$.

2. 1. 2. Spin Detectors: W and Bi_2Se_3

Tungsten (W) and bismuth selenide (Bi_2Se_3) were used for the conducting layer. In this thesis, W film is deposited by PLS-A, and Bi_2Se_3 film is grown by the molecular beam epitaxy (MBE) method.

W is one of the heavy-metal elements and its crystal structure is a body-centered cubic unit cell. Bulk W has a lattice constant of 3.1738 Å. This material has a spin Hall angle of ~0.50 due to the large spin-orbit interaction.

Bi_2Se_3 is a three-dimensional topological insulator (3D TI), with a Rhombohedral space group $R3m$. The material consists of five atomic layers (Se-Bi-Se-Bi-Se) connected by chemical bonds called a quintuple layer, bonded to other quintuple layers through van der Waals interactions. The unit cell spans across three quintuple layers with lattice constants $a = b$ = 4.156 Å, c = 28.736 Å, and γ = 120°.

Strong spin-orbit coupling in Bi_2Se_3 creates a band inversion, which together with time-reversal symmetry results in topologically protected surface states, while the bulk of the material is insulating with a bandgap of 0.3 eV. The surface states have a single Dirac cone with spin momentum locking. This prevents charge carriers from scattering back at impurities. The large spin orbit-coupling has also been shown to produce large spin Hall angles of 2−2.3[38].

2. 2. Mechanical Exfoliation

MPS_3 flakes were exfoliated on a 20 mm x 20 mm Si(001)/SiO2(50 nm) coupon with engraved markers for reference for the device fabrication. Before the mechanical exfoliation process, the resist on top of the substrates must be removed by submerging it in acetone and placing it into a 50 Hz sonication bath for 3 minutes.

Afterward, it was soaked in isopropanol (IPA) for 3 minutes. This cleaning step can be performed when the surface is free of any resist. Therefore, observe the surface of the substrate using an optical microscope to check whether the surface is clean or not. If some residues have remained on the surface, repeat the above cleaning procedures.

Exfoliation starts by placing an MPS_3 crystal on a strip of *Scotch® Magic™ Tape* or *3M™ Polyimide Film tape 7413T* and putting another one on top so the pieces stick together, interposing the crystal between them. The pieces were subsequently pulled apart, leaving MPS_3 on both pieces by mechanically cleaving the van der Waals forces holding the crystal together. This step can be repeated using the new thinner crystals, until eventually ~mono layers of MPS_3 are left on a piece of tape. Since the crystals can be quite small, the number of flakes can be increased by layering newly cleaved crystals on top of each other and offsetting it so more of the tape is covered with material. This can be repeated until a high enough density of material is obtained.

Once we obtain thin layers of MPS_3, with a high enough density to yield a good number of exfoliated flakes, the piece of tape is placed on top of the coupon such that the material touches the Si surface. Afterward, the tape is pulled back from the substrate, leaving flakes on top of the surface. This was done for separate samples of $MnPS_3$ and $CoPS_3$, but also combination samples were prepared by placing them on either half of the surface. After this procedure, submerge the coupon in IPA for 5 minutes to remove small parts of the flakes.

2. 3. Optical Microscopy (OM)

To find out and select the MPS_3 flakes which have a flat surface and quite thickness for device fabrication and Raman spectroscopy, 20 mm x 20 mm

Si(001)/SiO_2/MPS_3 coupons were prepared. Optical microscope (OM) measurements were conducted using a Microscope *OLYMPUS* Camera and *Olympus* System Microscope Model BX60. Images of exfoliated MPS_3 flakes were obtained from different magnifications. The most important is in this part, always keep the reference location with flakes together taking an image to align when fabricating the mask for devices. Then, image analysis was subsequently carried out using *Motic Images Plus Version 2.0 ML* software.

2. 4. Molecular Beam Epitaxy (MBE) Growth

To introduce the samples in the Molecular Beam Epitaxy (MBE) system for the TI growth, the 20 mm x 20 mm Si(001)/SiO_2/MPS_3 coupons were first glued to a 2-inch silicon carrier wafer. The carrier wafer was heated to 160 ºC on a hot plate and indium pellets (melting temperature of 156 ºC) were placed on top of it. Next, the Si(001)/SiO_2/MPS_3 sample was placed on top of the melted indium and subsequently cooled down for the indium to solidify again, sticking the Si(001)/SiO_2/MPS_3 sample to the carrier wafer.

The Bi_2Se_3 thin films were grown on MPS_3 flakes using the Plasma-Assisted Molecular Beam Epitaxy (PA-MBE) technique in a Riber MBE preparation module. Here, the Bismuth atomic flux is generated from a standard effusion cell while the metallic Selenium atomic flux is formed in a Radio Frequency (RF) plasma cell by the plasma cracking of pure H_2Se gas. Both molecular beams were simultaneously introduced in the growth chamber to form the Bi_2Se_3 thin films. The growth rate of the Bi_2Se_3 layer is set below 15 $nm\ h^{-1}$ and is entirely determined by the Bismuth beam rate. The H_2Se partial pressure can be varied between 1.0×10^{-6} Torr and 5.0×10^{-5} Torr in the plasma source, which results in a Se/Bi ratio typically larger than 100.

2. 5. Atomic Force Microscopy (AFM)

Atomic force microscope (AFM) measurements were carried out after exfoliation, MBE, EBL, and metallization steps. The measurements were performed using a *Dimension Edge*™ scanning probe microscope from Bruker consisting of a bidirectional (X-Y) motorized positioning stage, an SPM scan head with a nominal range of 90 μm x 90 μm, and a 5-mega pixel camera to inspect the surface during operation with a viewing are of 180 μm to 1465 μm. *Olympus* OMCL-AC160TS-R3 cantilevers with a resonance frequency ~300 kHz and a tip radius of 7 nm were used in a proximity tapping mode to probe the sample surface. To prevent further environmental interference, the microscope was placed inside an isolation chamber and on top of an air table to minimize vibrations. Subsequent data analysis of the images obtained from the AFM measurement was performed using the *WSxM* data analysis software.

2. 6. Raman Spectroscopy

Raman spectra measurements were performed after exfoliation (and MBE), using a *Horiba LabRAM HR Evolution Raman* tool with liquid N_2 stage. A 50LWDX Olympus objective was used to focus a 532 nm laser with a 25% ND filter on the sample with a spot size of ~1 μm in diameter. The scattered light from the sample was dispersed using 1800 grooves/mm grating and detected using a CCD with a 1000 μm confocal hole. Double exposure of 50 seconds was used to obtain the Raman spectra with a spike filter to remove cosmic spike filters. To investigate the magnetic transition of MPS_3 from paramagnetic to antiferromagnetic near the Néel temperature (T_N), Raman spectroscopy was carried out with a range of 298-78 K, and 100-600 cm^{-1} for $MnPS_3$, and $CoPS_3$ and 50-550 cm^{-1} for $FePS_3$.

2. 7. Device Fabrication

In this section, we contain the several steps needed to create a Hall bar and van der Pauw structure for electrical characterization of the pure MPS_3 and W/MPS_3 and to create a Hall bar with two-heaters structures for thermal-electrical characterization of the W/MPS_3. The process consists of three steps: digital design, electron beam lithography (EBL), and metallization.

2. 7. 1. Digital Design

The first step of the device fabrication process is the digital design. Optical images of MPS_3 flakes were obtained at several magnifications and inserted into *AutoCAD*® design software. Reference markers in optical images should be aligned with the digital design markers.

Once the images are correctly aligned in the digital design software, bond pads, contacts, windows, and heaters can be drawn. Bond pads of size 150 μm x 150 μm were used, while the contacts were drawn using polylines with a broader a starting from the flakes to the bond pads. Care was taken in the design of the contacts and bond pads such that they do not cover any large flakes or markers to prevent open circuits or peel-off after the EBL or metallization step. Windows would be covering the whole flake connecting the contacts. Using this process, both van der Pauw and Hall bar structures can be constructed. Furthermore, modify the contacts and heaters using *Klayout*® design software. Contacts can be a few lines with several widths of lines. Also, make sure the contacts have broader lines to reach out to the bond pads. Both sides of heaters should be parallel to each other to calculate the distance between heaters and parallel with contacts.

2. 7. 2 Electron Beam Lithography (EBL)

After the digital design, the bond pads, contacts, windows, and heaters were defined

through electron beam lithography (EBL). First, a 150 nm poly(methyl methacrylate) (PMMA), the electron beam resist, layer was deposited on top of the substrate surface by a spin coater with 2,000 rpm for 30 seconds, then bake at 165 ºC for 3 minutes.

Next, EBL was performed on the sample to define the features outlined in the digital design step, using a 250 μC/cm^2 dose for the contacts and a 300 μC/cm^2 dose for the bond pads in the case of pure MPS_3 samples. Apply 250 μC/cm^2 dose for the contacts and a 350 μC/cm^2 dose for the bond pads in case of W/MPS_3 samples. After EBL, the e-beam resist was developed by submerging the sample in a 1:1 mixed solution of methyl isobutyl ketone (MIBK) and isopropanol (IPA) for 30-60 seconds, and afterwards submerged into N-propanol to stop the development. If the development process did not produce clean-looking features, it was repeated until satisfied. Additionally, the step height of the features was measured using a profilometer or AFM.

2. 7. 3. Metallization

Following the EBL and development, metallization of the whole structure was performed, depositing a 5 nm Ti + 40 nm Au layer or 15 nm W. After that, the residual PMMA and metallization layers were removed through the lift-off process. This was both done by submerging the sample in acetone for up to 10 minutes at 50 ºC. After 5 minutes, the metalized surface on the side of the substrates was scratched away to further accelerate the lift-off process. At the end of the process, the residual resist and metallization layers were removed from the surface by locally agitating the solution at the sample surface using a pipet.

2. 8. Electrical Characterization

Electrical characterization of the devices was carried out in a *KEITHLEY 2400* and

Heliox system. There is no preparation for room-temperature measurements. Below steps are subsequential preparation for low-temperature measurements. First, the samples were cut into approximately 5 mm x 5 mm samples, making sure not to destroy any devices. The samples were subsequently glued to a chip with silver paste, and the device bond pads were wire bonded to the chip's bond pads. Next, the chip was attached to the sample holder and inserted into the sample chamber. The *Heliox* was then cooled to 7 K using liquid Helium. When completely cooled down, Hall effect measurements were carried out according to the Hall bar and van der Pauw method using a current of 1 μA. An out-of-plane and in-plane magnetic field for each $MnPS_3$ and $CoPS_3$ was applied to the sample ranging between -8 and 8 T. From these low-temperature measurements, the sheet resistance, carrier concentration, and carrier mobility could be determined. Also, from room-temperature measurements, the I-V curve and resistance can be obtained.

2. 9. Thermal-Electrical Characterization

Thermal-electrical characterization of the W/MPS_3 devices was carried out in a Heliox system. The preparation procedure is the same as the above electrical characterization. Apply the current to the heater, then calculate the ∇ T from the generated Δ T using a Joule heat. Then apply out-of-plane and in-plane magnetic fields for $MnPS_3$ and $CoPS_3$ each to generate the inverse spin Hall effect (ISHE). Finally, the generated voltage could be obtained from the electric field of ISHE with transverse direction to Δ T and magnetization.

3. Results and Discussion

3. 1. Flake analysis

3. 1. 1. Optical Microscopy (OM)

In the MPS_3 crystal system, transition metal, M (M=Mn, Co, and Fe) atoms are connected with six S atoms forming a honeycomb lattice, while P atoms are coordinated with three S atoms and one P atom to form a $[P_2S_6]^{4-}$ unit structure. Its crystal structure is shown in Figure 1. Figure 1(a) shows a top view of the MPS_3 structure, and Figure 1(b) shows a side view of the MPS_3 structure.

After the mechanical exfoliation of MPS_3 flakes, Some MPS_3 flakes were prepared with different thickness conditions to fabricate devices and measure the Raman spectroscopy. For the device fabrication, choosing a flake is better having quite a big size, without any flakes surrounding to prevent short. Also, the rectangular shape of the flake is good because it makes it to easier design the contacts of the mask for the Hall bar structure. If its shape is lozenge or triangular, it could be used as a van der Pauw structure. In general, MPS_3 flakes have flat surfaces and most of the flakes have micrometer range sizes.

Figure 2 shows the optical images of MPS_3 flakes in different thickness ranges. In the case of ~few layers MPS_3 flakes represent a gray color like a shadow. Between 10 to 30 nm of MPS_3 flakes are dark green color, then more light color up to ~50 nm of thickness. So, 50 nm of MPS_3 flakes have a light green color, then change yellow color. Therefore, about 70 nm of MPS_3 flakes have a pale yellow color. Larger than 100 nm thickness of MPS_3 flakes show the red color. Accordingly, the detailed thickness was analyzed using an atomic force microscope (AFM).

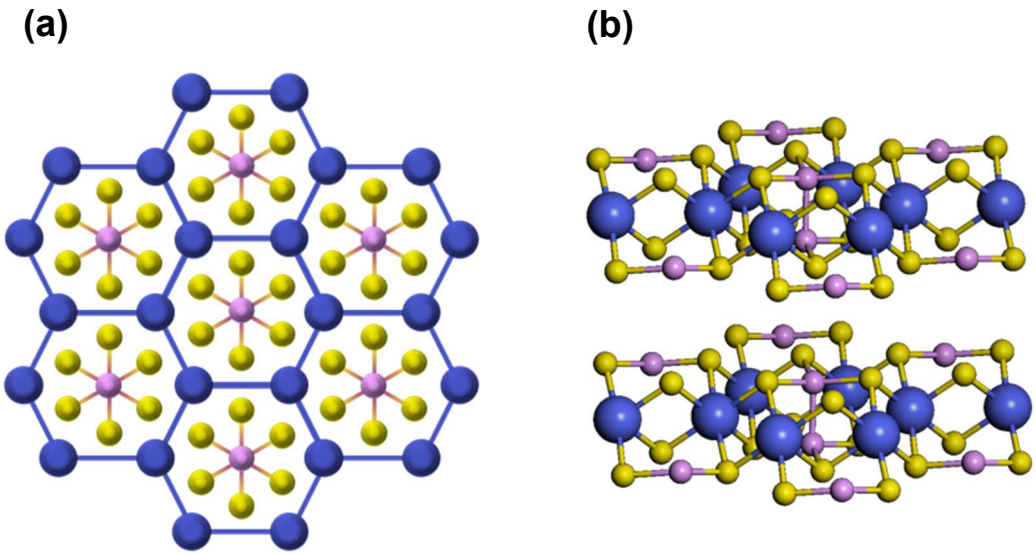

Figure 1. Crystal structure of MPS_3. (a) Top view and (b) side views of MPS_3 structures. Transition metal (M=Mn, Co, and Fe) atoms are blue, phosphorus atoms are violet, and sulfur atoms are yellow.

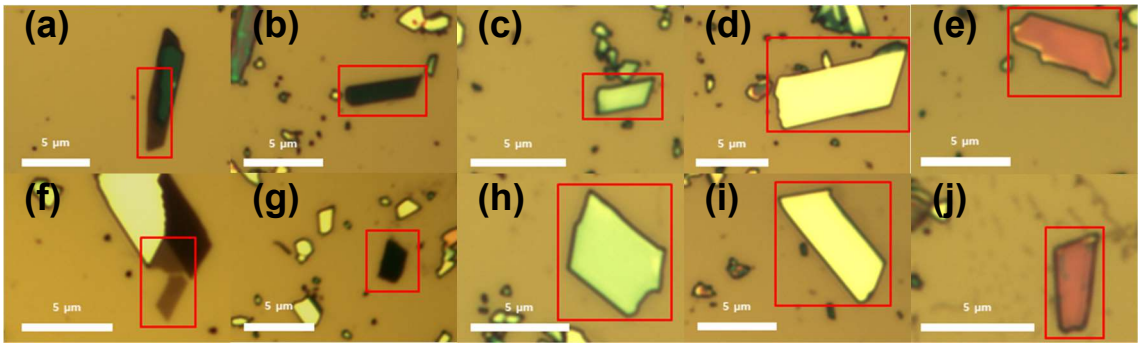

Figure 2. Optical images of MPS_3 having different thickness ranges. The individual flakes are obtained from (a, b, c, d, e) $MnPS_3$ and (f, g, h, i, j) $CoPS_3$. Flakes with a thickness (a, f) of less than 10 nm are gray, (b, g) between 10 and 30 nm are dark green, (c, h) of about 50 nm are light green, (d, i) of about 70 nm are pale yellow, and (e, j) larger than 110 nm are red.

3. 1. 2. Atomic Force microscopy (AFM)

Measurement for the exact thickness and size of each flake was conducted using AFM and its results are in Figure 3. We confirmed that MPS_3 flakes as a result of mechanical exfoliation have a nanometer range of thickness and micrometer range of scale. The thickness of flakes coincides with above mentioned various colors for $MnPS_3$ and $CoPS_3$. Profiling of MPS_3 flakes was performed along the flake orientation to determine more accurate thickness, and the results are inset in the AFM images of Figure 3. To measure the roughness of the surface of flakes, analysis of RMS roughness was carried out with a size of 1 μm x 1 μm flake using *WSxM* software. Its RMS roughness (Rq) is lower than 0.5 μm for both $MnPS_3$ and $CoPS_3$ flakes. The RMS roughness shows that each flake has a flat surface, suggesting that the MPS_3 flakes can be used as a substrate on which W will be deposited and on which Bi_2Se_3 can grow uniformly.

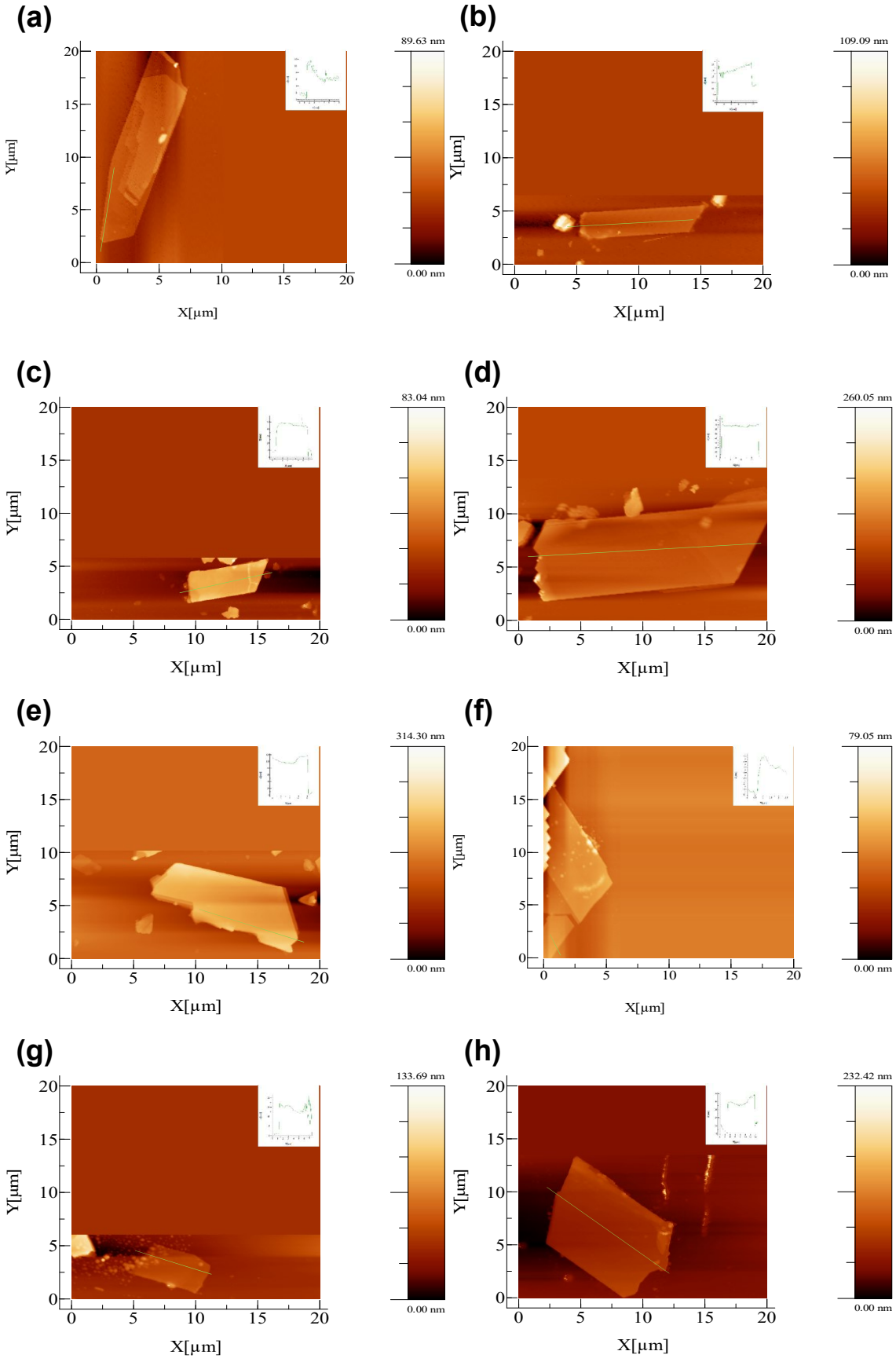
(a)
89.63 nm
0.00 nm
Y[µm]
X[µm]
(b)
109.09 nm
0.00 nm
Y[µm]
X[µm]
(c)
83.04 nm
0.00 nm
Y[µm]
X[µm]
(d)
260.05 nm
0.00 nm
Y[µm]
X[µm]
(e)
314.30 nm
0.00 nm
Y[µm]
X[µm]
(f)
79.05 nm
0.00 nm
Y[µm]
X[µm]
(g)
133.69 nm
0.00 nm
Y[µm]
X[µm]
(h)
232.42 nm
0.00 nm
Y[µm]
X[µm]

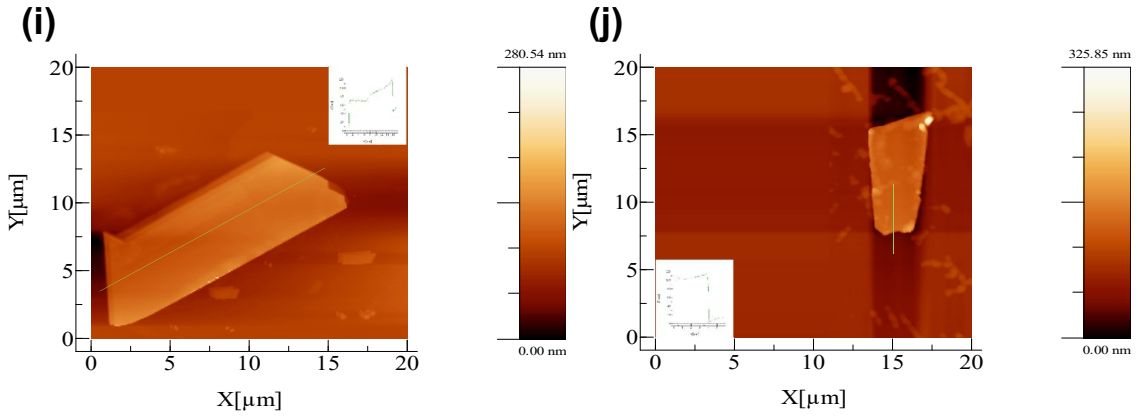

Figure 3. AFM images of MPS_3 with a different thickness ranges coinciding above Figure 2. The individual flakes are obtained from (a, b, c, d, e) $MnPS_3$ and (f, g, h, i, j) $CoPS_3$. The inset image shows profiling for green line in each AFM image.

3. 1. 3. Raman spectroscopy

Raman spectroscopy is a widely used non-destructive analysis method to explore the magnetism of 2D materials indirectly. 2D magnetic materials have their critical temperature where magnetic ordering has changed such as Curie temperature (T_C) of ferromagnets or Néel temperature (T_N) of antiferromagnets. It offers the possibility to observe magnetic ordering changes via peak changes when passing through T_C or T_N using Raman spectroscopy. Furthermore, antiferromagnets do not have a net magnetization, so it is impossible to measure their magnetic property directly using conventional tools, e.g., magneto-optical Kerr effect (MOKE) for the ferromagnets. There are many types of research about 2D magnetic materials that show magnetism in bulk state, even low dimensional state such as a few layers and monolayer. For example, it was already reported that Heisenberg-type $MnPS_3$ represents their antiferromagnetic property in the case of a few layers, even monolayer. Moreover, Raman spectroscopy offers a good platform for investigating temperature and thickness dependence towards 2D magnetic materials.

As shown in Figure 4(a), there are six peaks consisting of P_2 and P_4 to P_8 including the Si peak at 522 cm^{-1} in the range of 100-600 cm^{-1} for the bulk $MnPS_3$. These peaks are divided into low-frequency peaks and high-frequency peaks. Low frequency peaks, P_1 and P_2 peaks originated from the vibration of Mn atoms and high frequency peaks P_3 to P_8 are from the vibration of the $[P_2S_6]^{4-}$ bipyramidal structures. Although the P_1, P_3, and P_7 peaks were not observed in our measurement. The P_3 peak is a non-active A_{2g} mode. We could focus on the P_2 peak near 156 cm^{-1} to see the transition near the T_N in Figure 4(b). From the literature, the magnetic phase transition occurs when passing through the T_N. We observed the slightly blue shifted P_2 peak as temperature decreased, like a reported paper. Originally, the P_2 peak showed the blue shift above T_N and the red shift below T_N as temperature decreased, but our system's limitation temperature was 78 K, so we could not capture the red shift of the P_2 peak below T_N. Also, the P_2 peak shift is shown in Figure 4(c), as changing temperature at four

samples having a different thickness. The P_2 peak increases as temperature decreases reaching 100 K, and then a fluctuation occurs near the T_N. We checked that each peak decreased from 100 K, showing a red shift slightly in some cases. Furthermore, Figure 4(d) shows a Full Width at Half Maximum (FWHM) of the P_2 peak from the same condition as Figure 4(c). Each peak suffers a variation starting from 100 K. In the case of the $MnPS_3$ having 120 nm and 70 nm of thickness, FWHM rapidly increased near the T_N, it was the same as the already reported paper. So, we could anticipate that these pieces of evidence from the peak shift and FWHM of the P_2 peak mean a magnetic transition at its T_N without an additional decrease in the temperature.

Unlike Heisenberg-type $MnPS_3$, exploring about XY-type $CoPS_3$ has not been conducted widely. $CoPS_3$ has an in-plane magnetization, unlike the out-of-plane magnetization of $MnPS_3$. So, we want to investigate MPS_3 with different magnetization directions via Raman spectroscopy. Bulk $CoPS_3$, which has a Néel temperature (T_N) of 120 K, was analyzed in the same condition as $MnPS_3$, using Raman spectroscopy in Fig. 5(a). Bulk $CoPS_3$ represents eight peaks including the Si peak at the same position in the case of the $MnPS_3$. Low-frequency peaks P_1 and P_2 peaks originate from the vibration of Co atoms, and other high-frequency peaks are from the vibration of $[P_2S_6]^{4-}$ structure, same with $MnPS_3$. The P_3 peak is in non-active mode and the P_9 peak is not detected due to the weak intensity in our measurements condition. Therefore, we analyze the P_2 peak to investigate the magnetic ordering transition in Figure 5(b). Its P_2 peak is obtained from the bulk $CoPS_3$, showing a blue shift as decreasing temperature. This temperature dependence of the P_2 peak was reported in a paper, but there was a split P_2 peak due to the polarization Raman spectroscopy. Its split P_2 peak gets far away from each other as temperature decreases. So, our results coincide with one of the P_2 peaks from the reported paper showing the blue shift of the P_2 peak. Figure 5(c) shows the increasing P_2 peak shift as decreasing temperature in four $CoPS_3$ flakes having different thickness. Furthermore, the FWHM of the P_2 peak is shown in Figure 5(d) with the same condition as Figure 5(c). There

is a small fluctuation near the T_N in the case of $CoPS_3$ with 70 nm and 40 nm of thickness and it supports our claim that the magnetism changes in our measurement. Its FWHM value is minimized at the TN, and it recovered approaching 100 K. However, our P_2 peak region is different from the reported P_2 peak. Originally, the P_2 peak appeared at 149 cm^{-1}, but our P_2 peak appeared near 125 cm^{-1}. There would be a need for further research to clarify the difference.

$FePS_3$, which has an Ising type antiferromagnetic ordering has six peaks in the range of 50 to 450 cm^{-1} as Figure 6(a). Like other MPS_3, low frequency (P_1 and P_2) peaks from Fe atoms, and high frequency peaks (P_3 to P_6) from the vibration of $[P_2S_6]^{4+}$ structure. In this case, we don't need to consider the Si peak because the Si peak appears at about 520 nm^{-1}. Figure 6(b) shows the P_1 and P_2 peaks of bulk $FePS_3$ indicating a split of the P_1 peak and the appearance of the P_2 peak as temperature decreases. The reported T_N of $FePS_3$ is 123 K. So, we could confirm the red-shifted split of the P_1 peak below T_N. Figure 6(c) shows the P_1 peak shift and Figure 6(d) also shows the P_1 peak FWHM as temperature decreases. Unlike $MnPS_3$ and $CoPS_3$, $FePS_3$ represents a clear red shift as Figure 6(c). Additionally, we confirmed the magnetic transition near the T_N via FWHM of the P_1 peak from Figure 6(d). However, we tried to compare their thickness dependence using the low-frequency peaks, there is only a P_5 peak from the 14 nm of $FePS_3$. Most of the peaks are not distinguishable from the background signal, so we could not possibly fit it. So, the reason why there are only three types of thickness for $FePS_3$ in Figure 6(c, d).

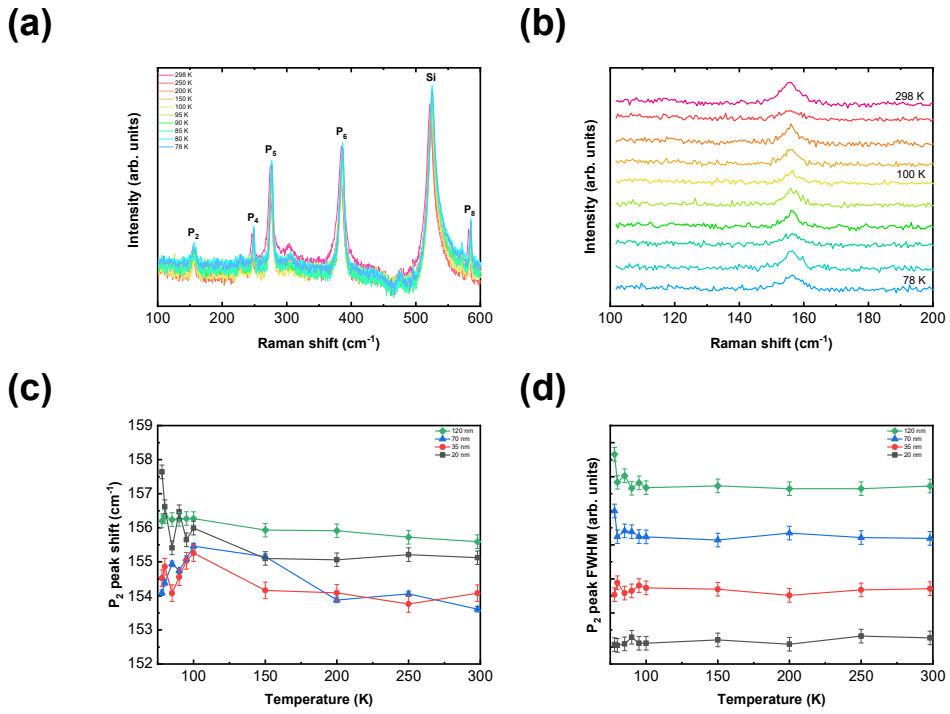

Figure 4. Raman spectrum of $MnPS_3$. (a) Overall spectrum of bulk $MnPS_3$ with various temperature. The P_2 peak (b) of bulk $MnPS_3$ as decreasing temperature, (c) shift, and (d) FWHM with different thickness.

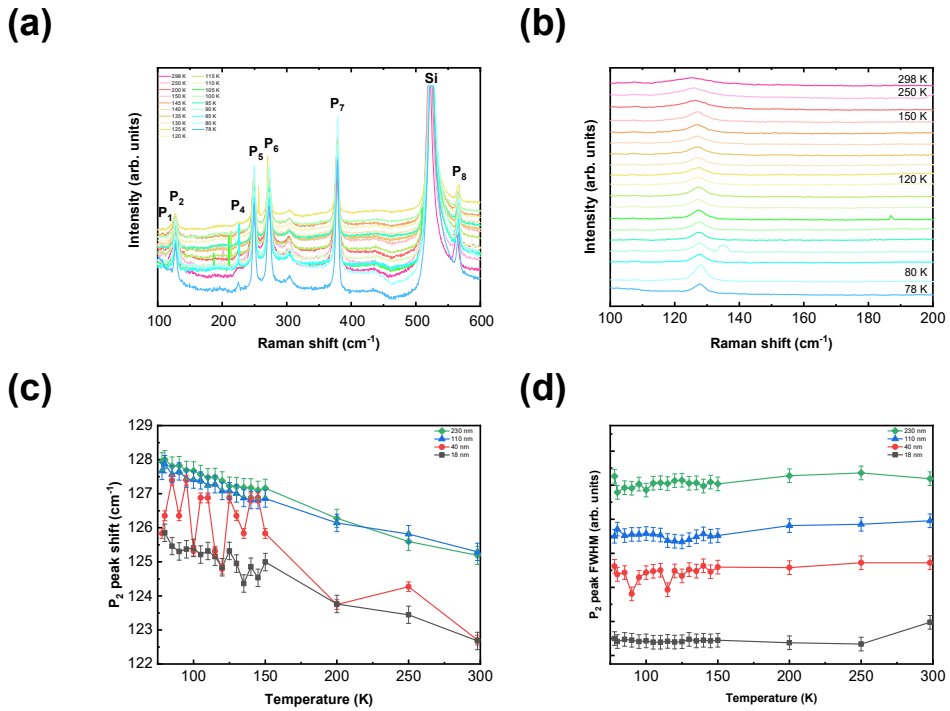

Figure 5. Raman spectrum of $CoPS_3$. (a) Overall spectrum of bulk $CoPS_3$ with various temperature. The P_2 peak (b) of bulk $CoPS_3$ as decreasing temperature, (c) shift, and (d) FWHM with different thickness.

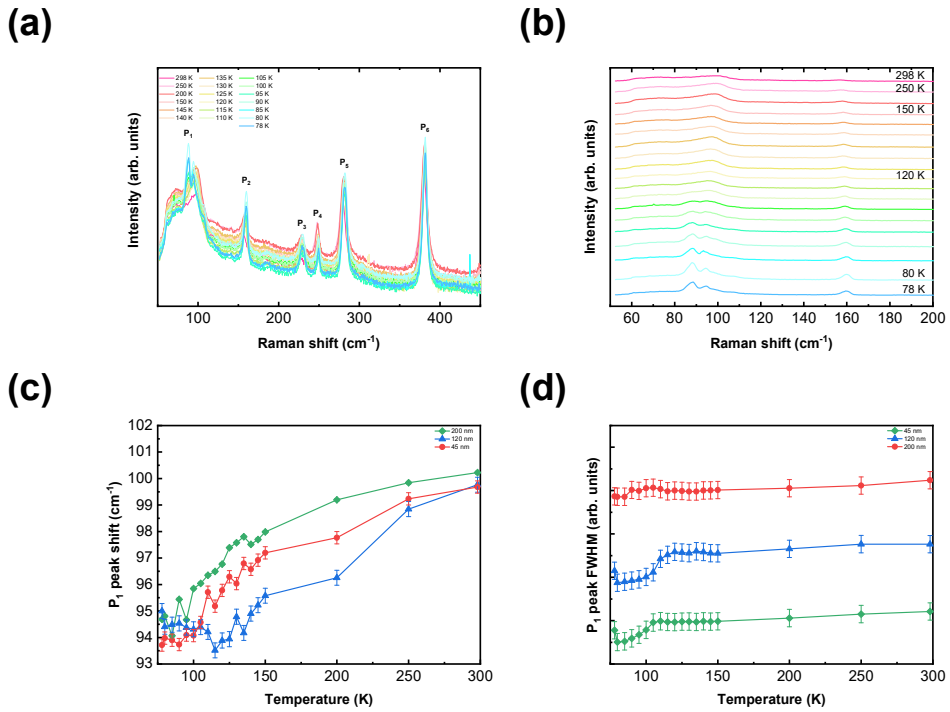

Figure 6. Raman spectrum of $FePS_3$. (a) Overall spectrum of bulk $FePS_3$ with various temperature. The P_1 peak (b) of bulk $FePS_3$ as decreasing temperature, (c) shift, and (d) FWHM with different thickness.

3. 2. Device Fabrication

3. 2. 1. E-beam Lithography (EBL)

We fabricated the digital design with optical images selected in the optical microscopy (OM) section. E-beam lithography was conducted after spin coating of E-beam resist using a digital design, then developed. We checked the development status using an OM after developing it for 30 seconds as shown in Figure 7(a). It shows an insufficient development which represents the remaining PMMA as a dark color near the contacts. So, we conducted additional development for 5 seconds to remove the remaining PMMA. Figure 7(b) shows well-developed devices and heaters after further development. To confirm the clear development for components of the device even considering the inside of heaters, we conducted AFM for them. Figure 8 shows the AFM images for contacts and heaters, which have about 120 to 130 nm of thickness. In these steps, we classify the devices that we can use or not. The devices which have the wrong alignment might have leakage of currents more than we expected. So, we should consider whether to use them or not.

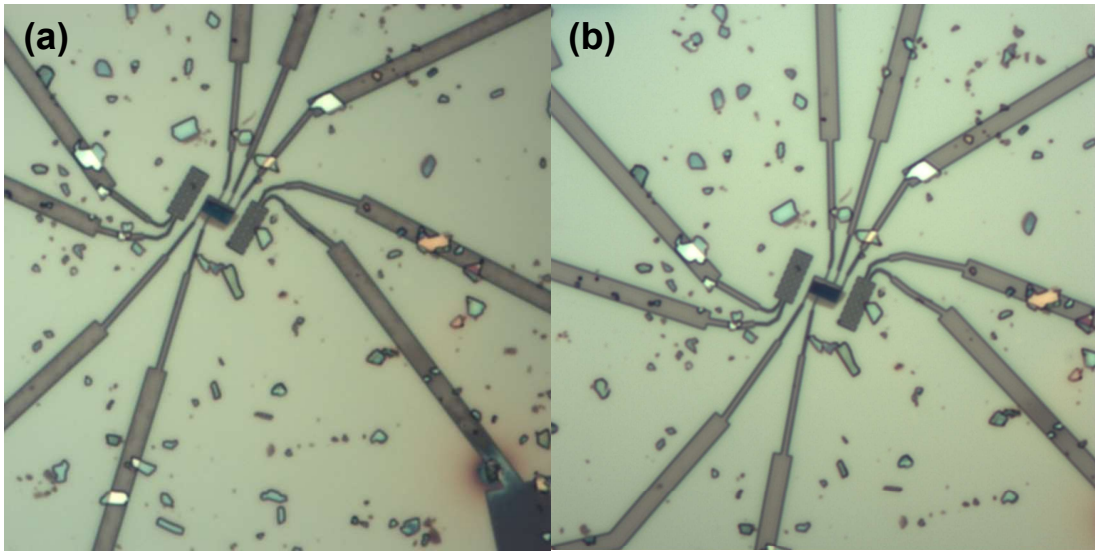

Figure 7. Optical images after the development of (a) 30 seconds having a remaining PMMA in the devices, and (b) a further 5 seconds without any PMMA.

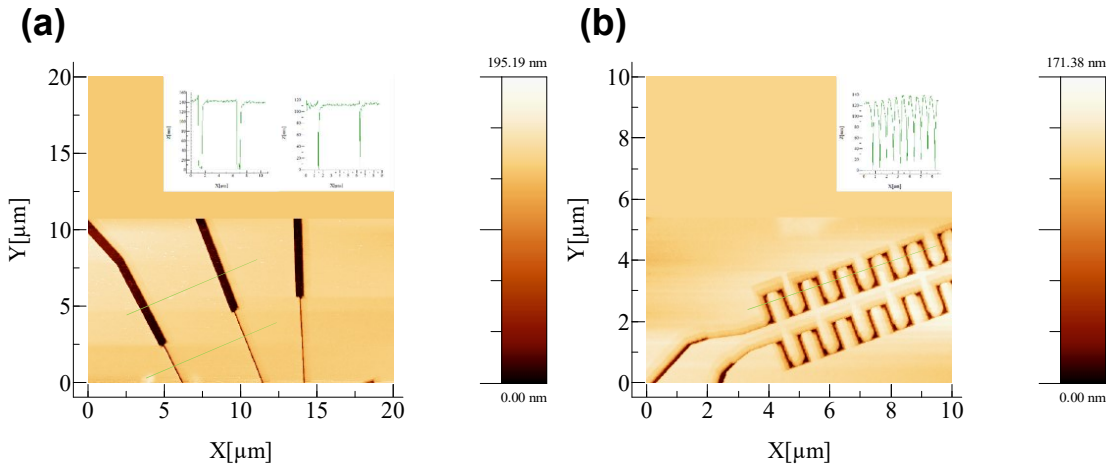

Figure 8. AFM images of (a) contacts, and (b) heaters after development. The depth of (a) contacts is 125±15 nm, and (b) heater is about 120 nm. The inset images represent a profiling of each line. (a) The left inset means the top line and the right inset means the bottom line.

3. 2. 2. Deposition of W

Next, we deposited 15 nm of W on the designed devices and then conducted a lift-off process to remove the remaining metal surrounding the devices. After the lift-off step, we should check whole devices using an OM and AFM. We can clarify the final shape of the devices and heaters and the thickness of the metal layer in Figure 9. Fig. 9(a) shows the optical image of the whole structure including both sides of the heaters, and Fig. 9(b) shows the AFM image of Fig. 9(a). From this AFM analysis, we demonstrate that the tungsten layer has a 15 nm thickness for devices and heaters. Also, the lift-off process to the inside of the heater was done well, indicating a closed circuit, and likely working well. Additionally, we analyze the morphology of the W/MPS_3 using an AFM in Figure 10. We compared MPS_3 and W/MPS_3 in order to check the morphology of the surface. Fig. 10(a, b) shows without tungsten, and Fig. 10(c, d) shows a W/MPS_3 surface. There is a clear difference between them, thus indicating that the tungsten deposition was also done properly on the MPS_3 flakes. Also, the RMS roughness of W/$MnPS_3$ and W/$CoPS_3$ are 0.5082 and 0.4167, showing higher values than without tungsten. But those are still low levels of roughness, indicating the possibility of application for further deposition or something on the surface.

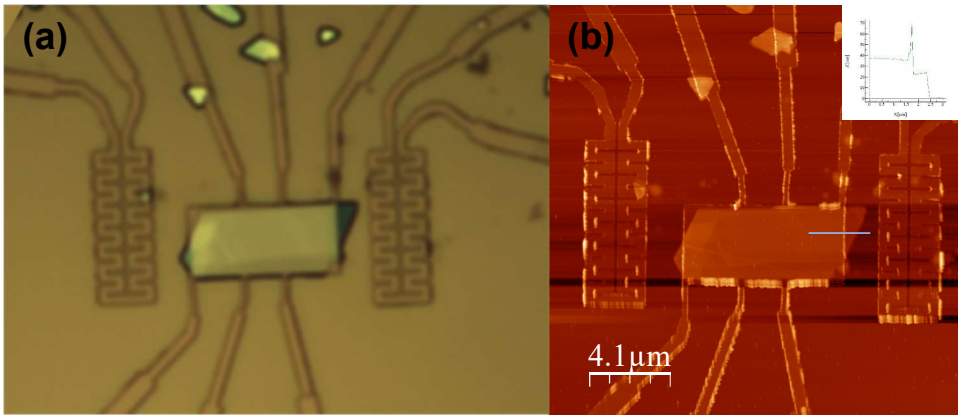

Figure 9. The whole device consists of heaters, window, and contacts for (a) OM image and (b) AFM image. The Inset image shows the thickness between the W window and the MPS_3 flake, and the MPS_3 flake and Si/SiO_2 surface.

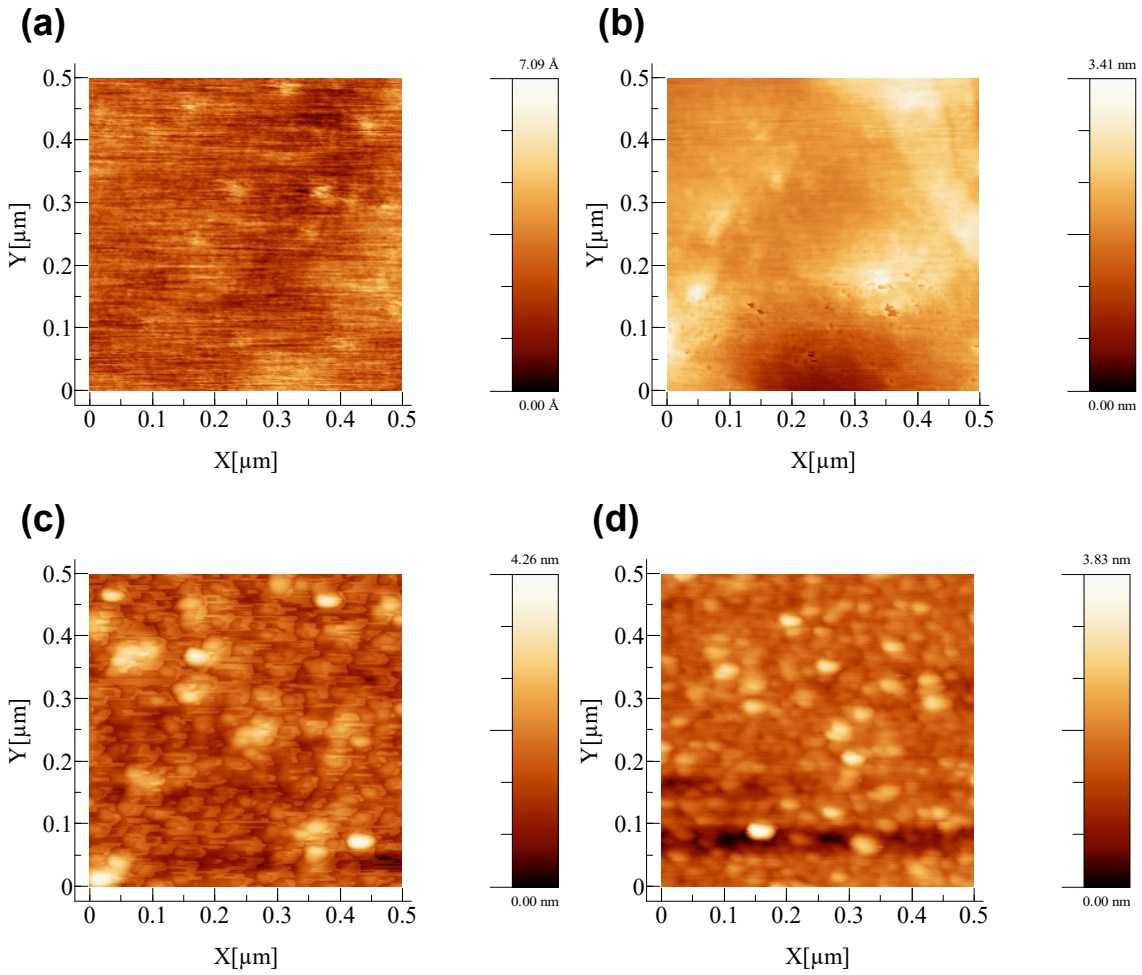

Figure 10. AFM images of (a) $MnPS_3$, (b) $CoPS_3$, (c) W/$MnPS_3$, and (d) W/$CoPS_3$. (a, b) The surface of the MPS_3 flakes shows flat morphology. (c, d) Each W/MPS_3 shows W grains on the MPS_3 surface.

3. 3. Electrical Characterizations

First, room-temperature (RT) measurements were carried out to check the resistance of heaters and devices before low-temperature measurements. Some heaters and devices were analyzed, indicating some errors because there are some shorted devices caused by contacting bulk MPS_3 flake. The heater generated linear currents as voltage signals as shown in Figure 11. Applied voltages are 0 to 0.3 V and 0 to -0.2 V for Figure 11(a, b), then generated currents are 4 μA at 0.3 V and 3 μA at -0.2 V. However, there is a huge resistance than what we expected. Theoretically, our heater structure has a total length of 31.4×10^{-6} m, and its width is 0.4×10^{-6} m. W electrical resistance (**ρ**) is 5.6×10^{-8} Ω-m (at 293 K), and deposited W thickness is about 15×10^{-9} m. So, we can calculate the resistance of heaters using the below equation.

$$R = \rho \times \frac{l}{a}$$

From this equation, we can anticipate the resistance should be about 300 Ω. But the resistance that we obtained was tens of thousands of ohms. We expect that the W layer is too thin, so bond pads were damaged while measuring RT measurements. So, additional study is in progress to confirm the issue and solve it. Then, further thermal-electrical measurements via a low-temperature system will be considered.

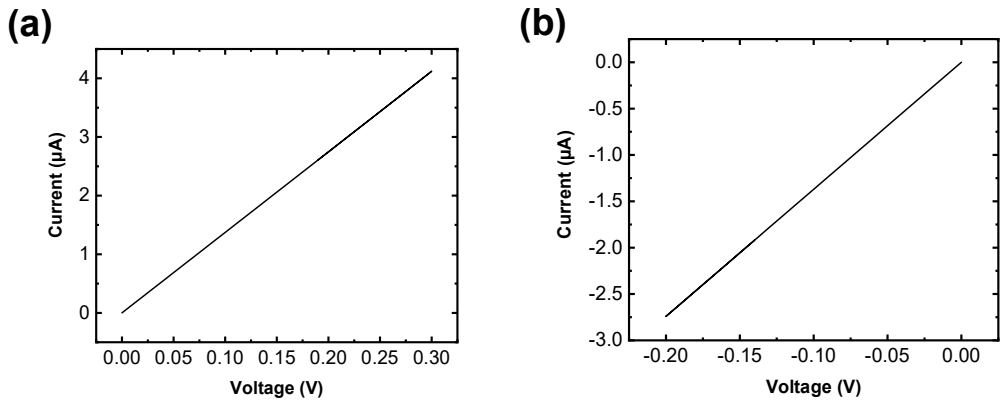

Figure 11. I-V curve with 0.05 A for different voltage ranges of (a) 0 to 0.3 V, and (b) 0 to -0.2 V.

4. Conclusion

In this thesis, we report the spin caloritronic device, which could improve the inverse spin Hall effect (ISHE) from the thermal-induced spin-wave spin currents (SWSC), consisting of 2D antiferromagnetic MPS_3 with W. Antiferromagnetism from the exfoliated MPS_3 flakes is determined by Raman spectroscopy, indicating each magnetic transition as temperature and thickness dependence. The W/MPS_3 device was fabricated through a series of processes using E-Beam Lithography (EBL) and deposition. Before confirming the spin Seebeck effect (SSE) and ISHE, room temperature measurements were performed and the resistance values were outside the expected range, so further studies are being performed.

This research was supported by the MOTIE (Ministry of Trade, Industry, and Energy) in Korea, under the Fostering Global Talents for Innovative Growth Program (P0017312) supervised by the Korea Institute for Advancement of Technology (KIAT)

References

(1) Williams, A. J.; Torquato, M. F.; Cameron, I. M.; Fahmy, A. A.; Sienz, J. Survey of energy harvesting technologies for wireless sensor networks. *IEEE Access* **2021**, *9*, 77493-77510.
(2) Uchida, K.-i.; Adachi, H.; Kikkawa, T.; Kirihara, A.; Ishida, M.; Yorozu, S.; Maekawa, S.; Saitoh, E. Thermoelectric generation based on spin Seebeck effects. *Proc. IEEE* **2016**, *104* (10), 1946-1973.
(3) Zoui, M. A.; Bentouba, S.; Stocholm, J. G.; Bourouis, M. A review on thermoelectric generators: Progress and applications. *Energies* **2020**, *13* (14), 3606.
(4) Baibich, M. N.; Broto, J. M.; Fert, A.; Van Dau, F. N.; Petroff, F.; Etienne, P.; Creuzet, G.; Friederich, A.; Chazelas, J. Giant magnetoresistance of (001) Fe/(001) Cr magnetic superlattices. *Phys. Rev. Lett.* **1988**, *61* (21), 2472.
(5) Uchida, K.-I.; Takahashi, S.; Harii, K.; Ieda, J.; Koshibae, W.; Ando, K.; Maekawa, S.; Saitoh, E. Observation of the spin Seebeck effect. *nature* **2008**, *455* (7214), 778-781.
(6) Seki, S.; Ideue, T.; Kubota, M.; Kozuka, Y.; Takagi, R.; Nakamura, M.; Kaneko, Y.; Kawasaki, M.; Tokura, Y. Thermal generation of spin current in an antiferromagnet. *Phys. Rev. Lett.* **2015**, *115* (26), 266601.
(7) Sharma, H.; Wen, Z.; Mizuguchi, M. Spin Seebeck effect mediated reversal of vortex-Nernst effect in superconductor-ferromagnet bilayers. *Sci. Rep.* **2023**, *13* (1), 4425.
(8) Bauer, G. E.; Saitoh, E.; Van Wees, B. J. Spin caloritronics. *Nat. Mater* **2012**, *11* (5), 391-399.
(9) Mizuguchi, M.; Nakatsuji, S. Energy-harvesting materials based on the anomalous Nernst effect. *STAM* **2019**, *20* (1), 262-275.
(10) Sharma, H.; Wen, Z.; Takanashi, K.; Mizuguchi, M. Anomaly in anomalous Nernst effect at low temperature for C1b-type NiMnSb half-Heusler alloy thin film. *JJAP* **2019**, *58* (SB), SBBI03.
(11) Saitoh, E.; Ueda, M.; Miyajima, H.; Tatara, G. Conversion of spin current into charge current at room temperature: Inverse spin-Hall effect. *Appl. Phys. Lett.* **2006**, *88* (18).
(12) Uchida, K.-I. Transport phenomena in spin caloritronics. *PJA-B* **2021**, *97* (2), 69-88.
(13) Yan, W.; Sagasta, E.; Ribeiro, M.; Niimi, Y.; Hueso, L. E.; Casanova, F. Large room temperature spin-to-charge conversion signals in a few-layer graphene/Pt lateral heterostructure. *Nat. Commun* **2017**, *8* (1), 661.
(14) Safranski, C.; Barsukov, I.; Lee, H. K.; Schneider, T.; Jara, A.; Smith, A.; Chang, H.; Lenz, K.; Lindner, J.; Tserkovnyak, Y. Spin caloritronic nano-oscillator. *Nat. Commun* **2017**, *8* (1), 117.
(15) Meier, D.; Reinhardt, D.; Van Straaten, M.; Klewe, C.; Althammer, M.; Schreier, M.; Goennenwein, S. T.; Gupta, A.; Schmid, M.; Back, C. H. Longitudinal spin Seebeck effect contribution in transverse spin Seebeck effect experiments in Pt/YIG and Pt/NFO. *Nat. Commun* **2015**, *6* (1), 8211.
(16) Uchida, K.-i.; Adachi, H.; Ota, T.; Nakayama, H.; Maekawa, S.; Saitoh, E. Observation of longitudinal spin-Seebeck effect in magnetic insulators. *Appl. Phys. Lett.* **2010**, *97* (17).
(17) Wu, S. M.; Zhang, W.; Amit, K.; Borisov, P.; Pearson, J. E.; Jiang, J. S.; Lederman, D.; Hoffmann, A.; Bhattacharya, A. Antiferromagnetic spin Seebeck effect. *Phys. Rev. Lett.* **2016**, *116* (9), 097204.
(18) Susner, M. A.; Chyasnavichyus, M.; McGuire, M. A.; Ganesh, P.; Maksymovych, P. Metal thio-and selenophosphates as multifunctional van der Waals layered materials. *Adv Mater* **2017**, *29* (38), 1602852.
(19) Wang, F.; Shifa, T. A.; Yu, P.; He, P.; Liu, Y.; Wang, F.; Wang, Z.; Zhan, X.; Lou, X.; Xia, F. New frontiers on van der Waals layered metal phosphorous trichalcogenides. *Adv. Funct. Mater.* **2018**, *28* (37), 1802151.
(20) Samal, R.; Sanyal, G.; Chakraborty, B.; Rout, C. S. Two-dimensional transition metal phosphorous trichalcogenides (MPX 3): a review on emerging trends, current state and future perspectives. *J. Mater. Chem.* **2021**, *9* (5), 2560-2591.
(21) Peng, J.; Chen, Z.-j.; Ding, B.; Cheng, H.-M. Recent Advances for the Synthesis and Applications of 2-Dimensional Ternary Layered Materials. *Res.* **2023**, *6*, 0040.

(22) Rahman, S.; Torres, J. F.; Khan, A. R.; Lu, Y. Recent developments in van der Waals antiferromagnetic 2d materials: Synthesis, characterization, and device implementation. *ACS nano* **2021**, *15* (11), 17175-17213.
(23) Du, K.-z.; Wang, X.-z.; Liu, Y.; Hu, P.; Utama, M. I. B.; Gan, C. K.; Xiong, Q.; Kloc, C. Weak van der Waals stacking, wide-range band gap, and Raman study on ultrathin layers of metal phosphorus trichalcogenides. *ACS nano* **2016**, *10* (2), 1738-1743.
(24) Morin, F. Oxides which show a metal-to-insulator transition at the Neel temperature. *Phys. Rev. Lett.* **1959**, *3* (1), 34.
(25) Soumyanarayanan, A.; Reyren, N.; Fert, A.; Panagopoulos, C. Emergent phenomena induced by spin–orbit coupling at surfaces and interfaces. *Nature* **2016**, *539* (7630), 509-517.
(26) Demasius, K.-U.; Phung, T.; Zhang, W.; Hughes, B. P.; Yang, S.-H.; Kellock, A.; Han, W.; Pushp, A.; Parkin, S. S. Enhanced spin–orbit torques by oxygen incorporation in tungsten films. *Nat. Commun* **2016**, *7* (1), 10644.
(27) Wang, Y.; Deorani, P.; Banerjee, K.; Koirala, N.; Brahlek, M.; Oh, S.; Yang, H. Topological surface states originated spin-orbit torques in Bi 2 Se 3. *PRL* **2015**, *114* (25), 257202.
(28) Hasan, M. Z.; Kane, C. L. Colloquium: topological insulators. *RMP* **2010**, *82* (4), 3045.
(29) Ando, Y. Topological insulator materials. *JPSJ* **2013**, *82* (10), 102001.
(30) Wang, Y.; Zhu, D.; Wu, Y.; Yang, Y.; Yu, J.; Ramaswamy, R.; Mishra, R.; Shi, S.; Elyasi, M.; Teo, K.-L. Room temperature magnetization switching in topological insulator-ferromagnet heterostructures by spin-orbit torques. *Nat. Commun* **2017**, *8* (1), 1364.
(31) Nagaosa, N. A new state of quantum matter. *Sci.* **2007**, *318* (5851), 758-759.
(32) Konig, M.; Wiedmann, S.; Brune, C.; Roth, A.; Buhmann, H.; Molenkamp, L. W.; Qi, X.-L.; Zhang, S.-C. Quantum spin Hall insulator state in HgTe quantum wells. *Sci.* **2007**, *318* (5851), 766-770.
(33) Zhang, Y.; He, K.; Chang, C.-Z.; Song, C.-L.; Wang, L.-L.; Chen, X.; Jia, J.-F.; Fang, Z.; Dai, X.; Shan, W.-Y. Crossover of the three-dimensional topological insulator Bi2Se3 to the two-dimensional limit. *Nat. Phys.* **2010**, *6* (8), 584-588.
(34) Cho, S.; Butch, N. P.; Paglione, J.; Fuhrer, M. S. Insulating behavior in ultrathin bismuth selenide field effect transistors. *Nano Lett.* **2011**, *11* (5), 1925-1927.
(35) Mazumder, K.; Shirage, P. M. A brief review of Bi2Se3 based topological insulator: from fundamentals to applications. *J. Alloys Compd.* **2021**, *888*, 161492.
(36) Chuai, Y.-H.; Zhu, C.; Yue, D.; Bai, Y. Epitaxial Growth of Bi2Se3 Infrared Transparent Conductive Film and Heterojunction Diode by Molecular Beam Epitaxy. *Front. Chem.* **2022**, *10*, 847972.
(37) Zhan, L.-B.; Yang, C.-L.; Wang, M.-S.; Ma, X.-G. Two-dimensional Bi2Se3 monolayer with high mobility and enhanced optical absorption in the UV–visible light region. *Physica E Low Dimens. Syst. Nanostruct.* **2020**, *124*, 114272.
(38) Lu, Q.; Li, P.; Guo, Z.; Dong, G.; Peng, B.; Zha, X.; Min, T.; Zhou, Z.; Liu, M. Giant tunable spin Hall angle in sputtered Bi2Se3 controlled by an electric field. *Nat. Commun* **2022**, *13* (1), 1650.